This is a preprint, the final version is subject to change, of the American Mineralogist (MSA)
Cite as Authors (Year) Title. American Mineralogist, in press.
DOI: https://doi.org/10.2138/am-2020-7125

American Mineralogist

Revision 2

Petrographic and Spectral Study of Hydrothermal Mineralization in Drill Core from Hawaii: A potential analogue to alteration in the Martian subsurface

Wendy M. Calvin[1], Nicole Lautze[2], Joe Moore[3], Donald Thomas[2], Eric Haskins[2], Brandon P. Rasmussen[1],

[1]Department of Geological Sciences, University of Nevada, Reno, NV 89577, USA

wcalvin@unr.edu; rasmussen.brandon.geo@gmail.com

[2]Hawaii Institute of Geophysics and Planetology, University of Hawaii, Honolulu, HI 96822, USA

lautze@hawaii.edu; dthomas@soest.hawaii.edu; haskins@hawaii.edu

[3]Energy and Geoscience Institute, University of Utah, Salt Lake City, UT, 84108

jmoore@egi.utah.edu

This is a preprint, the final version is subject to change, of the American Mineralogist (MSA)
Cite as Authors (Year) Title. American Mineralogist, in press.
DOI: https://doi.org/10.2138/am-2020-7125

Abstract

Continuous rock core was collected for 1764 m (5786') on the Pohakuloa Army Training base near the center of the big island of Hawaii. The core traverses basaltic lava flows from the volcano's shield building phase and perched aquifers and higher temperature groundwaters were encountered. The collected samples record water-rock interactions of basaltic materials in a setting that may be a model for groundwater interactions on Mars. We collected visible and infrared point spectra of materials in the lowest portion of the core where alteration was noted to become more prominent. We identified three types of phyllosilicate spectral signatures and three types of zeolites. The phyllosilicates show similarity to those identified on Mars using data from the Compact Reconnaissance Imaging Spectrometer for Mars (CRISM). Based on the field survey, 25 depths were selected for sampling and petrographic analysis of thin sections. The spectral data and thin section work have strong agreement in the types of materials identified by the two different techniques. Both the spectral and petrographic data indicate low to moderate temperature geothermal alteration occurred in the lower half of the core. The field spectra are a useful reconnaissance tool for selecting mineralogic diversity for subsequent higher resolution and more time consuming laboratory analysis.

Keywords: IR spectroscopy, aqueous alteration, Hawaii drill core, geothermal

This is a preprint, the final version is subject to change, of the American Mineralogist (MSA)
Cite as Authors (Year) Title. American Mineralogist, in press.
DOI: https://doi.org/10.2138/am-2020-7125

Introduction

Hawaii has long been studied as a Mars analog, both for its volcanic geology and also because early telescopic data showed palagonite (a poorly crystalline alteration product of basaltic tephra) was a reasonable analog to the average Martian spectrum (e.g. Singer 1982; Bell et al. 1993). As with Mars, the Hawaiian volcanic stratigraphy records a basaltic crust interstratified with basaltic sediments and weathered basaltic soil profiles. Several previous studies have used airborne imaging spectroscopy to map surface alteration for comparison to Mars orbital spectral data (Guinness et al. 2007; Seelos et al. 2010). Additional field studies have explored the spectral properties of alteration products formed in the desert surface environments of Hawaii (e.g. Bishop et al 2007; Minitti et al. 2007; Chemtob et al. 2010). These previous studies have exclusively examined surface alteration as an analog to Mars. Given recent reports of long-lived and widespread Martian groundwaters (Andrews-Hanna et al. 2010; Ehlmann et al. 2011; Michalski et al. 2013) the subsurface of Hawaii represents a crucial little-explored analog.

Between 1989 and 1999 five drill holes were made on the island of Hawaii to assess geothermal energy development potential and to examine volcanic geology expressed in the young shield areas (e.g. Moore and Trusdell 1993; Garcia et al. 2007). Science Observation Holes (SOH) 1, 2, and 4 were drilled into the Kilauea Eastern Rift Zone and the Hawaii Scientific Drilling Project (HSDP) drilled two deep holes near Hilo (Figure 1) (Bargar et al. 1995; Quane et al. 2000; Garcia et al. 2007). All these drill holes are near the coastal margins and substantially penetrate volcanic strata that were erupted subaerially but are now below sea level. Alteration observed in the SOH holes is influenced by sea water (Bargar et al. 1995, 1996), as well as temperatures up

to 350°C. Site selection of the HSDP project was designed to avoid the rift zones in order to minimize alteration (Garcia et al. 2007). Alteration in HSDP2 was mild to moderate and mostly in the intervals of submarine hyaloclastites (Garcia et al. 2007). In contrast, the drill core that we examined in this study was drilled in the center of the island (Figure 1) and did not reach submarine elevations, so that alteration is not expected to be driven by marine fluids but rather ground water or past subaerial exposure. The core thus provides an analog for surface or subsurface alteration on Mars, that is now exposed via erosion or impact gardening. Prior studies also have not collected data for the entire core length, but only of representative sections using cut samples from various lithologic units. Our field survey was designed to collect frequent measurements over a large depth interval.

In 2007 geophysical field surveys conducted across the Humu'ula Saddle Region between the Mauna Kea and Mauna Loa volcanoes identified subsurface conductive formations that were likely associated with the presence of high elevation groundwater over broad regions (Pierce and Thomas 2009). In 2013 the Army Garrison and Office of Naval Research supported drilling a continuously-cored test hole over one conductive feature to define the local hydrologic conditions. The drill location is on the Pohakuloa Training Area (PTA) (Figure 1) and the core hole PTA-2 started at an absolute elevation of 1946 m (6385') and drilled down 1764 m (5786') to reach an absolute elevation of 182 m (599'). The core traverses various subaerial lava flows, representing the shield-building phase of the island and ages that are quite young, < 300,000 years old (Pierce and Thomas 2009). The lithology is dominantly basalt with varying amounts of plagioclase and olivine phenocrysts (Figures 2 and 3). Both pāhoehoe and 'a'ā textures are identified as well as some explosive units, scoria, ash, glass and a few sedimentary units and

intrusions (see also Jerram et al. 2019). Visual logging of PTA-2 during drilling noted that discontinuous alteration became prevalent starting at ~ 1 km depth. A sequence of shallow perched aquifers at local-ambient temperatures were encountered but were underlain by the regional water table beginning ~ 600m depth, showing considerably higher temperatures that increased with depth. At the bottom of the hole equilibrium temperatures exceeded 140°C and the lowest 700 m of the hole showed a temperature gradient of ~165°C/km. Deeper rocks showed progressive secondary mineralization with depth. Fluid chemistry in the local aquifer at 300 m depth was generally dilute and the Na-K and Na-K-Ca geothermometers yielded apparent equilibrium temperatures in the range of 250°C to 260°C (Thomas et al. 2015).

The moderate to intermediate temperatures are representative of those expected in hydrothermal systems that might have developed around impact craters or in groundwater-volcanic interactions in the subsurface of Mars. The young ages are a proxy for short-lived or limited water-rock action early in the history of Mars (Ehlmann et al. 2011; Michalski et al. 2013; Bishop et al. 2018). In May of 2014 we collected visible and infrared spectra using our portable Analytical Spectral Devices (ASD) field spectrometer. The ASD wavelength range is sensitive to many hydrothermal alteration minerals that are of interest in geothermal exploration. Calvin and Pace (2016) used this technique to identify alteration in geothermal drill core from locations in Nevada and Alaska and found good correlation to pre-existing XRD results that were performed on limited samples from those cores. Our survey was focused on the alteration products in order to understand in more detail how the alteration temperature and environments may vary down hole. Secondary mineralization can indicate the presence, chemistry, and temperature of hydrothermal fluids, therein helping to characterize a present and/or past geothermal system.

Finally, the drill core samples provided the opportunity to perform a reconnaissance survey that would frequently sample the alteration zones and identify mineralogic diversity for subsequent higher resolution and more time consuming laboratory analysis. Additional detailed analysis of these samples is provided in the companion paper by Rasmussen et al. (in revision).

Drill Core Material and Methods

The hole was drilled from March to June of 2013. During drilling, core boxes were imaged with scale bars, color chips and markers of box depth and notes were used to create a lithologic log (Figure 2). Figure 3 shows a typical image of a core box. Archive photos are available on the Hawaii Groundwater & Geothermal Resources Center (HGGRC) web site provided in the reference list. After logging, the core boxes were wrapped in plastic and stored in a container on the PTA Military Reservation near the drill site. In May of 2014 we visited the drill site in order to collect spectra with our portable field instrument. We triaged boxes from the storage container for the deeper portions and with a team of four moved boxes from the storage container to a table for measurement (Figure 4). Detailed note taking during acquisition recorded the spectrum number collected, the core box number, and location within the core box so that accurate depth could be associated with each spectrum. We collected 780 spectra over the core depth interval from 972 to 1763 m (3190’ to 5785’) over 3 days of field work.

We used an ASD field spectrometer, with an attached contact probe (Figure 4). In this configuration, the instrument uses an internal halogen light source to measure reflected light over wavelengths from 0.4 to 2.5 μm. The spectrum is collected over a circular area ~ 15 mm in

diameter. Spectra are acquired on the outer (rounded) edge of core and if the core is naturally split, spectra of interior faces may be obtained. The ASD instrument is calibrated against a halon plate at the start of and periodically throughout data collection, so that data are reported in reflectance for direct comparison with established mineral spectral library standards. The field operator makes real-time decisions on whether or not to target specific locations, or to measure at a fixed interval. This survey was focused on secondary alteration products and spots for data collection focused on visually obvious alteration with occasional collection of unaltered matrix.

Following the methods of Calvin and Pace (2016) individual spectra are converted into an image "cube" where spectra are vertically sorted in depth order and both expert analysis and methods used to map mineralogy in remote sensing images can be used to identify the mineralogy of the core. Due to the spot size of the spectroradiometer, spectra are typically combinations of several minerals. Thus, at a particular depth, several minerals might be identified due to multiple diagnostic features. We associate common spectral types with known alteration minerals or mineral assemblages using established spectral libraries (e.g. Baldridge et al. 2009; Kokaly et al. 2017). We first identify common spectral patterns to use as "endmembers" and then use these to map other depth locations where similar features occur. Methods to map the vertical distribution of spectral types include a matched filter (MF), spectral angle map (SAM), and various color combinations and decorrelation stretch (DCS) products focused on specific mineral absorption features as described by Calvin and Pace (2016).

Based on core log and spectral data, 25 depths were sampled by cutting 7 mm thick cross sections of the core (Table 1). Pieces of these cross sections were then made into thin sections

for petrographic analysis. Using standard 30 micron thin sections, all samples were analyzed using cross-polarized (XP), transmitted, and reflected light, on a polarizing light petrographic microscope, with a magnification of up to 200x. Basic mineralogy was established using growth habits and crystal form, pleochroism, birefringence, relief, and indices of refraction, and then compared to established mineral parameters (Nesse 2013). Once individual minerals were known, cross cutting relationships and growth zonation of alteration minerals were identified and noted. Eight of the thick cut sections (noted in Table 1) were subject to additional analyses as described by Rasmussen et al. (in revision).

Results

Common Spectral Features

Based on our past work with geothermal drill core we identified eight common spectral types in the measurements on the PTA-2 core and these form our set of endmembers as shown in Figure 5. Our endmember spectra include unaltered or slightly altered mafic minerals, Mg/Fe phyllosilicates, and three spectral types associated with zeolites. Figure 5 spectra are selected single measurements that best represent the distinct spectral features of those mineral endmembers. Figure 5a shows the common mafic patterns (e.g. Hunt and Salisbury, 1970; Adams, 1974; Gaffey et al., 1993). The red spectrum is typical of augite, with the broad 1.0 μm feature characteristic of pyroxenes. The blue spectrum has this feature and a broader absorption up to 1.7 μm that is associated with olivine. Both spectra show broad absorptions from 1.8 to 2.4 μm with a peak near 2.15 μm as shown by the vertical line. These features are not associated

with any known mafic minerals but are common in the basaltic rock samples in the JPL spectral library (Baldridge et al. 2009; Figure 5a). For comparison, an average of 6 naturally occurring basalts in the JPL library is shown as the black spectrum. This library spectrum exhibits similar features although the peak between the two absorptions occurs at a slightly lower wavelength than in our measurements. These features may arise from pore water or other minor components in the natural basalts that are not seen in the mineral separates used for the spectral libraries.

Figure 5b shows the prevalent phyllosilicate spectra observed. Calvin and Pace (2016) found that a band triplet including mineral mixtures of muscovite, illite, chlorite, clinochlores, and epidote was common in high temperature alteration of basalts and andesites from Akutan, AK, and dacites at Blue Mountain, NV. The temperatures reached in the PTA-2 hole are not as high as these other localities and we don't identify chlorite or epidote. In the PTA-2 survey phyllosilicates are interpreted as saponite or other Mg/Fe smectites, potentially talc and serpentines. A double feature phyllosilicate (green line in Figure 5b) was originally interpreted as clinochlore, but the 1.4 and 1.9 μm features do not match, and ultimately, we concluded there is no good analog in any of the libraries. This material was subject to detailed additional analysis as described by Rasmussen et al. (in revision). The phyllosilicates show similar absorption features to those found on Mars. They exhibit features near 2.30 μm (vertical line in Figure 5b) that shift in band center and some have additional weak features near 2.25 and 2.40 μm. These features of the Fe/Mg phyllosilicates are attributed to variability in Fe/Mg/Al content.

Figure 5c notes the three spectral types of zeolites found in the survey. Many zeolites are similar in spectral shape with broad features at 1.4 and 1.9 μm and the purple (lowest) line in

Figure 5c is consistent with stilbite, heulandite or clinoptilolite. The magenta (middle) line exhibits an additional feature near 1.8 μm (vertical line) and the spectral shape is characteristic of analcime. The red (upper) spectrum shows strong absorptions from water in the mineral structure and a "stair step" like decrease in reflectance toward longer wavelengths that is similar to natrolite or scolecite zeolites, although the features in those minerals are narrower than what we observed in PTA-2. Phillipsite, the zeolite identified using XRD (Rasmussen et al., in revision) is not available in either the USGS or JPL spectral libraries. During drilling it was noted that some of the zeolites encountered were quite highly hydrated – they had, initially, a waxy/soapy texture (which caused problems with drilling) and, when dried, they lost a substantial fraction of their mass and turned to powder. Hence part of the spectral mismatch may be due to dehydration as well as lack of representative samples in the common spectral libraries.

The eight spectral types noted in Figure 5 were then mapped within the depth ordered spectral cube (Figure 6). In Figure 6, each row represents one field spectral measurement. However, spectra were not acquired linearly with depth so that there is not a direct correlation to the lithology of Figure 2. Based on the spectral diversity we selected 25 locations to acquire cut sections for further analysis (horizontal lines on the far right of Figure 6, noted by depth in feet, and Table 1) so these depths provide the link to Figure 2 that also shows sample locations. Mapped endmember colors are linked to those in Figure 5, mafics are red and blue, phyllosilicates green and cyan and zeolites in shades of purple. Areas that are not mapped (black) don't provide a strong match to any specific endmember and are mixtures. The companion paper by Rasmussen et al (in revision) provides detailed linear unmixing of the field

spectra. Eight of the cut sections (blue horizontal lines) were examined at high resolution as described by Rasmussen et al. (in revision) with additional analysis using SEM and XRD.

We note that alteration was not linear with depth; instead some zones were more highly altered than others, exhibiting deeper alteration features and a lack of primary mafic absorptions, and zones of differing alteration were identified as shown in Figure 6. We also measured the cut faces of the thick sections and compared these to the spectra obtained on the exterior of the core. Figure 7 demonstrates that the spectra from the cut face and the field data are in good agreement regarding the dominant spectral features, and Table 1 summarizes the spectral features for each of the 25 sampled locations. In most cases, changes in overall albedo between the field and cut face data are due to variation in the material in the field of view. For Figure 7c, the much stronger features in the field data are because that spectrum was taken of an alteration coated fracture face.

Petrographic Analysis

Over 200 photomicrographs were taken across the 24 thin sections representing a depth from 977 to 1761 m (3206 to 5777 feet). Figure 8 shows a select few of these photomicrographs. The number below each image is the depth of sample; in parentheses is the image width, the scale bar is 0.5mm in each image. All images shown are in crossed polarizers (XP) except 8j, and listed in increasing depth. In Figure 8a – 977 m (3206 ft) the groundmass consists of plagioclase (plag) laths, orthopyroxene (opx), and oxides. There are some large plag phenocrysts and one notable larger hexagonal opx (left), and one large olivine (olv) phenocryst in the image center with a

minor iddingsite alteration halo or rim. Figure 8b – 1125 m (3691 ft) exhibits a groundmass of plag laths, opx, and oxides. Smectite alteration is observed surrounding a vug and heavily altered olv crystals in the image center. On the right an opx mineral appears to be resorbed. Figure 8c – 1346 m (4417 ft) shows an altered fine grained groundmass with vugs that are completely infilled with fibrous zeolite. Figure 8d – 1346 m (4417 ft) also shows a highly altered, fine grained groundmass with two distinct zeolites filling in the vug at the center of the image. Cross cutting relationships indicate the tabular zeolite formed first. In Figure 8e – 1379 m (4524 ft) a heavily altered groundmass consists of amorphous silica, oxides, and smectite. The vugs are filled with smectite, zeolite, and distinct high birefringence phase (pink tones) that may be calcite or prehnite. In Figure 8f – 1451 m (4763 ft) the heavily altered groundmass consists of oxides, plag, and amorphous silica. Infilling the large vug is stilbite, a planar zeolite and a fibrous zeolite. Figure 8g – 1463 m (4799 ft) illustrates a heavily altered olivine-rich groundmass with vugs filled by smectite and multiple zeolites. Figure 8h – 1567 m (5140 ft) shows a highly altered groundmass with multiple resorbing phenocrysts. Again, vugs are infilled with smectite and zeolites. Figure 8i – 1680 m (5511 ft) shows a less altered groundmass of plag, opx, and olv with vugs lined with iddingsite. Figure 8j – 1736 m (5696 ft - 50x) not in XP, shows moderately altered ground mass. The image was selected to show green alteration lining the vugs, and green alteration of an olivine crystal, at the bottom and middle right of the image, which may be chlorite. Figure 8k – 1736 m (5696 ft - 120x) shows large feldspar laths and a moderately altered rock with resorbed olivine crystals. The alteration pattern between feldspar laths does not appear to be smectite, and may be pumpellyite or fibrous chlorite. Figure 8l – 1761 m (5777 ft) shows a groundmass of plag, opx, olv, and rich in oxides. A large phenocryst of olv appears at

the lower right of the image and alteration to iddingsite is exhibited in the large mineral grain on the left side of image. There is smectite lining veins.

Some general conclusions from the petrographic analysis are that the smectite is ubiquitous; however whether any interlayered illite/smectite is present is uncertain. Olivine is variably altered to iddingsite. Stilbite, clinoptilolite and other, particularly fibrous, zeolites are common. Calcite is expected as an infilling of vugs in one section. Analcime, quartz/chalcedony and chlorite were suspected through this analysis but were not confidently identified.

Discussion

In general, the spectral data and thin section work strongly agree in the materials identified by the two different techniques. Plagioclase is essentially featureless at ASD wavelengths, but both techniques identified olivine and pyroxene as the unaltered starting materials. The thin section work identified iddingsite, which is a term used for a fine-grained mixture of smectite, chlorite, and iron oxides (e.g. Barker, 2014) and is consistent with alteration products seen in the infrared spectra (Fe/Mg smectites and an unidentified phyllosilicate). In two locations, SR-513 (4524 ft) (Figure 8e) and SR-631 (5696 ft) (Figure 8j,k), unique phases were identified in thin section. In SR-513 a high- birefringent phase was identified and tentatively identified as calcite or prehnite. In SR-631 at 20x magnification (Figure 8k) the alteration did not appear to be smectite but pumpellyite or a fibrous chlorite. The spectral data did not identify any carbonate, nor did we identify any moderately higher temperature minerals (prehnite, pumpellyite or chlorite). As shown by Rasmussen et al. (in revision), at high resolution, using SEM elemental analysis and XRD, most alteration is identified as zeolitic or Mg-saponite.

Both the spectral and petrographic data indicate low to moderate temperature geothermal alteration occurred in the lower half of the core. Smectite clay forms across a temperature range from 70 - 180°C, and the zeolites (e.g. stilbite) indicate alteration temperatures of ~125°C (e.g. Chamley, 1989; Ehlmann et al., 2011; Michalski et al., 2015; Viennet et al. 2017; Bishop et al., 2018). Spectrally, the majority of zeolites are similar to each other, however analcime and natrolite-like zeolites were uniquely identified; these also form at low to moderate temperatures. Epidote, a higher temperature mineral (~250°C), was not observed in either dataset. However, iddingsite (identified petrographically) may indicate temperatures at or above 180 °C. As described in the introduction, the fluid chemistry from a shallow perched aquifer indicates higher equilibrium temperatures than the mineral assemblages identified in the regional aquifer in the lowest portion of the hole, surveyed in our work. This suggests that the regional aquifer is not connected to shallower perched lenses. Given the overlapping alteration of different types of zeolite (Figure 8d), it is possible that two or more stages of alteration occurred. Also, the zones of differing alteration (Figure 6) may suggest different episodes or temperatures as well as variability in the starting mafic mineralogy (which was not examined) and availability of olivine which was noted to vary as shown in Figure 2.

Implications

While Mars has numerous alteration locations identified from orbital data, the majority of the surface is dominated by primary igneous mineralogy, including wide-spread olivine (e.g. Ehlmann and Edwards 2014). In the PTA-2 core, unaltered olivine and pyroxene phenocrysts

316 occur in the groundmass adjacent to highly altered vugs and are preserved throughout the section
317 surveyed. Given the limited alteration and abundant preservation of olivine to depths of 1.5 km
318 the core may be representative of subsurface alteration in moderate pH environments on Mars,
319 now exposed via erosion or exhumed through impact processes. Similar alteration might occur
320 at the Martian surface with limited water exposure. Alteration identified in the core is also
321 spectrally similar to alteration minerals observed by the Compact Reconnaissance Imaging
322 Spectrometer for Mars (CRISM) (e.g. Ehlmann et al. 2011). Fe/Mg smectites, a primary
323 alteration product of the PTA-2 core is often found on Mars and is the most common alteration
324 phase identified in CRISM data (e.g. Ehlmann and Edwards 2014; Michalski et al. 2015).
325 Zeolites, the other common alteration phase observed in the PTA-2 core, are rare on Mars
326 (Ehlmann et al. 2011), and typically only identified as analcime, by the unique absorption feature
327 at 1.8 μm (Figure 5, pink spectrum). Where analcime has been identified on Mars, it occurs with
328 Fe/Mg smectites, as seen in PTA-2. This suggests that zeolites may be more common on Mars,
329 but are not observed in CRISM data due to the fact that the strong 1.4 and 1.9 μm absorption
330 features overlap with other many other hydrated minerals. Alternately, zeolites may form, but
331 become dehydrated or be altered themselves in the current Martian surface environment. Zeolites
332 have been proposed to be a component of the global fine grained dust on Mars (Ruff 2004).
333
334 The field spectral survey rapidly identified alteration signatures and the spatial locations of
335 distinct spectra, hence this is a useful reconnaissance tool for selecting mineralogic diversity for
336 subsequent higher resolution and more time consuming analysis. The spectra on the outside of
337 the core sample are representative of the cut face of the cross section of the core interior.
338 Differences in albedo and feature strength don't cause significant changes in mineral mapping

and/or interpretations. Field spectra always represent mineral mixtures, although, as is the case in Rasmussen et al., (in revision); they show the same features as higher resolution data but with weaker absorption features. This implies that weak features in CRISM data at 18m spatial scales are representative of small outcrops or mineral populations within the pixel.

A second hole was drilled in Fall of 2015. KMA-1 started at an elevation of 1645 m (5397') and reached a depth of 1528m (5014'). Currently funded work from NASA Solar System Workings will explore differences in alteration between the two holes, variations in mafic mineralogy with depth, potentially uncovering interleaved Mauna Kea and Mauna Loa flows and relate alteration environments to those found on Mars.

Acknowledgements

This project was funded in part by the Department of Energy awards: FG36-02ID14311 and 10EE0003997 to the Great Basin Center for Geothermal Energy for travel and data analyses. Additional support from the University of Nevada, Reno and the NASA Solar Systems Workings program Award #80NSSC19K0031 to WM Calvin. We appreciate the two external reviews whose comments and suggestions help improve the clarity of the manuscript.

References

Adams, J.B. (1974) Visible and near-infrared diffuse reflectance spectra of pyroxenes as applied to remote sensing of solid objects in the solar system. Journal of Geophysical Research, 79, 4829-4836.

Andrews-Hanna, J.C., Zuber, M.T., Arvidson, R.E., and Wiseman, S.M. (2010) Early Mars hydrology: Meridiani playa deposits and the sedimentary record of Arabia Terra. Journal of Geophysical Research-Planets, 115.

Baldridge, A.M., Hook, S.J., Grove, C.I., and Rivera, G. (2009) The ASTER spectral library version 2.0. Remote Sensing of Environment, 113(4), 711-715.

Bargar, K.E., Keith, T.E.C., Trusdell, F.A., Evans, S.R., and Sykes, M.L. (1996) Hydrothermal alteration mineralogy of SOH drill holes, Kilauea East Rift Zone geothermal area, Hawaii. USGS Open-File Report 96-0010.

Bargar, K.E., Terry, E., and Trusdell, F.A. (1995) Fluid-inclusion evidence for past temperature fluctuations in the Kilauea East Rift Zone geothermal area, Hawaii. Geothermics, 24(5-6), 639-659.

Barker, A. J. (2014) A Key for Identification of Rock-Forming Minerals in Thin Section, 173 p. CRC Press.

382 Bell, J.F., Morris, R.V., and Adams, J.B. (1993) Thermally altered palagonitic tephra - A spectral
383 and process analog to the soil and dust of Mars. Journal of Geophysical Research-Planets,
384 98(E2), 3373-3385.
385
386 Bishop, J.L., Schiffman, P., Murad, E., Dyar, M.D., Drief, A., and Lane, M.D. (2007)
387 Characterization of alteration products in tephra from Haleakala, Maui: A visible-infrared
388 spectroscopy, Mossbauer spectroscopy, XRD, EMPA and TEM study. Clays and Clay Minerals,
389 55(1), 1-17.
390
391 Bishop, J.L., Fairén A.G., Michalski J.R., Gago-Duport L., Baker L.L., Velbel M.A., Gross C.,
392 and Rampe E.B. (2018) Surface clay formation during short-term warmer and wetter conditions
393 on a largely cold ancient Mars. Nature Astronomy, 2, 206-213.
394
395 Calvin, W.M., and Pace, E.L. (2016) Mapping alteration in geothermal drill core using a field
396 portable spectroradiometer. Geothermics, 61, 12-23.
397
398 Chamley, H. (1989) Clay Sedimentology. 623 p. Springer-Verlag, New York.
399
400 Chemtob, S.M., Jolliff, B.L., Rossman, G.R., Eiler, J.M., and Arvidson, R.E. (2010) Silica
401 coatings in the Ka'u Desert, Hawaii, a Mars analog terrain: A micromorphological, spectral,
402 chemical, and isotopic study. Journal of Geophysical Research-Planets, 115.
403

Ehlmann, B. L., and Edwards, C. S. (2014). Mineralogy of the Martian Surface. *Annual Review of Earth and Planetary Sciences*. https://doi.org/10.1146/annurev-earth-060313-055024.

Ehlmann, B.L., Mustard, J.F., Murchie, S.L., Bibring, J.P., Meunier, A., Fraeman, A.A., and Langevin, Y. (2011) Subsurface water and clay mineral formation during the early history of Mars. Nature, 479(7371), 53-60.

Gaffey, S.J., McFadden L.A., Nash D., and Pieters C.M. (1993) Ultraviolet, visible, and near-infrared reflectance spectroscopy: Laboratory spectra of geologic materials. In C. M. Pieters and P. A. J. Englert, Eds., Remote Geochemical Analysis: Elemental and Mineralogical Composition, 43-77. Cambridge University Press. Cambridge.

Garcia, M.O., Haskins, E.H., Stolper, E.M., and Baker, M. (2007) Stratigraphy of the Hawaii Scientific Drilling Project core (HSDP2): Anatomy of a Hawaiian shield volcano. Geochemistry Geophysics Geosystems, 8.

Guinness, E.A., Arvidson, R.E., Jolliff, B.L., Seelos, K.D., Seelos, F.P., Ming, D.W., Morris, R.V., and Graff, T.G. (2007) Hyperspectral reflectance mapping of cinder cones at the summit of Mauna Kea and implications for equivalent observations on Mars. Journal of Geophysical Research-Planets, 112(E8).

HGGRC Core Photo web site: https://www.higp.Hawaii.edu/hggrc/projects/humuula-groundwater-research-project/hgrp-photos/, last accessed October 17, 2019.

Hunt, G.R. and Salisbury J.W. (1970) Visible and near-infrared spectra of minerals and rocks: 1. Silicate minerals. Modern Geology, 1, 283-300.

Jerram, D.A., Millett, J.M., Kück, J., Thomas, D., Planke, S., Haskins, E., Lautze, N., and Pierdominici, S. (2019) Understanding volcanic facies in the subsurface: a combined core, wireline logging and image log data set from the PTA2 and KMA1 boreholes, Big Island, Hawai`i. Sci. Dril., 25, 15-33.

Kokaly, R.F., Clark, R.N., Swayze, G.A., Livo, K.E., Hoefen, T.M., Pearson, N.C., Wise, R.A., Benzel, W.M., Lowers, H.A., Driscoll, R.L., and others. (2017) USGS spectral library version 7. US Geological Survey.

Michalski, J.R., Cuadros, J., Niles, P.B., Parnell, J., Rogers, A.D., and Wright, S.P. (2013) Groundwater activity on Mars and implications for a deep biosphere. Nature Geoscience, 6(2), 133-138.

Michalski, J. R., Cuadros, J., Bishop, J. L., Darby Dyar, M., Dekov, V., and Fiore, S. (2015). Constraints on the crystal-chemistry of Fe/Mg-rich smectitic clays on Mars and links to global alteration trends. *Earth and Planetary Science Letters*. https://doi.org/10.1016/j.epsl.2015.06.020

Minitti, M.E., Weitz, C.M., Lane, M.D., and Bishop, J.L. (2007) Morphology, chemistry, and spectral properties of Hawaiian rock coatings and implications for Mars. Journal of Geophysical Research-Planets, 112(E5).

Moore, R.B., and Trusdell, F.A. (1993) Geology of Kilauea Volcano. Geothermics, 22(4), 243-254.

Nesse, W.D. (2013) Introduction to Optical Mineralogy, 384 p. Oxford University Press

Pierce, H.A., and Thomas, D.M. (2009) Magnetotelluric and audiomagnetotelluric groundwater survey along the Humu'ula portion of Saddle Road near and around the Pohakuloa Training Area, Hawaii. Open-File Report.

Quane, S.L., Garcia, M.O., Guillou, H., and Hulsebosch, T.P. (2000) Magmatic history of the East Rift Zone of Kilauea Volcano, Hawaii based on drill core from SOH 1. Journal of Volcanology and Geothermal Research, 102(3-4), 319-338.

Rasmussen, B.P., Calvin, W.M., Ehlmann, B.L., Lautze, N., Fraeman, A.A., Bristow, T.S., and DesOrmeau, J.W. (in revision with Am Min) Characterizing Low-temperature Aqueous Alteration of Mars-Analog Basalts from Mauna Kea at Multiple Scales.

Ruff, S. W. (2004). Spectral evidence for zeolite in the dust on Mars. *Icarus*. https://doi.org/10.1016/j.icarus.2003.11.003

Seelos, K.D., Arvidson, R.E., Jolliff, B.L., Chemtob, S.M., Morris, R.V., Ming, D.W., and Swayze, G.A. (2010) Silica in a Mars analog environment: Ka'u Desert, Kilauea Volcano, Hawaii. Journal of Geophysical Research-Planets, 115.

Singer, R.B. (1982) Spectral evidence for the mineralogy of high-albedo soils and dust on Mars. Journal of Geophysical Research, 87(NB12), 159-168.

Thomas, D., Haskins, E., Wallin, E., and Pierce, H. (2015) New insights into structural controls affecting groundwater flow within an ocean island volcano, Mauna Kea, Hawaii, V21A-4731, AGU Fall Meeting, San Francisco, CA, Dec 14-18.

Viennet, J.-C., Bultel, B., Riu, L., and Werner, S.C. (2017). Dioctahedral Phyllosilicates Versus Zeolites and Carbonates Versus Zeolites Competitions as Constraints to Understanding Early Mars Alteration Conditions. Journal of Geophysical Research: Planets. https://doi.org/10.1002/2017je005343

Figure Captions

Figure 1: Location of historical drill holes and the PTA-2 hole used in this study on the island of Hawaii. Inset shows a close-up of the PTA-2 drill location near the Pohakuloa Army base near the center of the island.

Figure 2: Lithologic log for the lower section of the PTA-2 hole surveyed. Shades of gray to dark green record the level of olivine phenocrysts. Grey has no olivine, light green is sparse (1-2%), medium green is moderate (3-10%) and dark green is high (>10%). Blue flags note sample locations for cut sections in this work. Orange stars are potential explosive deposits. Orange lines indicate sedimentary units.

Figure 3: Example core box image depth ~3688' (1124 m). Logged as moderate plagioclase olivine-phyric basalt.

Figure 4: Field photo of spectral data collection set up.

Figure 5: Common spectral features identified – a) mafics, b) phyllosilicates, c) zeolites. See the text for a description of features and their mineral assignments. Vertical bars call out additional features described in the text.

Figure 6: Depth profile of best single mineral match to the field data. Field data are shallower to deeper, top to bottom and left to right. Because the field spectra are non-linear with depth, the horizontal bars note where cut sections were taken and correspond to Figure 2 and Table 1.

These bars are noted with depth in feet. Color of mapped mineral matches the colors in Figure 5 (red/blue = mafics, shades of green and cyan = phyllosilicates, pink and purple are zeolites). The blue horizontal bars are the locations of cut sections with additional analysis in the companion paper by Rasmussen et al. (in revision) also noted in Table 1. Black areas are mixtures that are modeled in detail in Rasmussen et al. (in revision).

Figure 7: Spectra of cut section faces (dotted, lighter lines) compared with original field data (solid lines) at the same depth. Panels are for (a) unaltered material (blue line in Figure 5a), (b) phyllosilicate (green line in Figure 5b), (c) phyllosilicate (cyan line in Figure 5b), (d) analcime (zeolite, pink line in Figure 5c), and (e) "stair step" zeolite (brown line in Figure 5c). For panel (c) the much stronger features in the field data are because that spectrum was taken of an alteration coated fracture face.

Figure 8: Photomicrographs of thin sections from core samples. The number below each image represents sample depth below the ground surface in meters. In parentheses is the image width, representing magnifications from 25x to 200x. The yellow bar in each frame is 0.5 mm wide. See the text for representative features.

Tables

Table 1:

Cut Section Depths and Samples selected for Additional Analysis

Sample ID	**Scan**	**Core**	**Depth in**	**Initial Interpretation**	**Thin**	**Additional**

	#	Box	m (ft)	Cut Face Spectrum	Section - See text for complete description.	Analysis and Dominant XRD* Minerals
SR 373-5.4	395	785	977.3 (3206.4)	Unaltered pyroxene	Fig 8a, plag, opx	pyx, plag
SR 392-8.9	439	805	1032.3 (3386.9)	Unaltered pyroxene w/ olivine component		pyx, plag, olv ✓
SR 422-1.3	521	836	1119.0 (3671.3)	Phyllosilicate, broad 2.2, strong 2.32		2:1 clay, olv, pyx, plag
SR 425-3.5	533	838	1125.2 (3691.5)	Phyllosilicate, broad 2.2, strong 2.32	Fig 8b, plag opx, smectite	2:1 clay, olv, pyx, plag ✓
SR 437-1.3	564	848	1153.5 (3784.3)	Similar to previous (422, 425)		2:1 clay, olv, pyx, plag

SR 446-6.8	596	857	1177.4 (3862.8)	Phyllosilicate, narrow, 2.245 strong 2.317		2:1 clay, pyx, plag
SR 459-3.1	630	870	1215.9 (3989.1)	Phyllosilicate, narrow, 2.245 strong 2.317		2:1 clay, pyx, plag ✓
SR 465-5.2	650	877	1235.1 (4052.2)	Unaltered pyroxene, weak alteration like 425		2:1 clay, pyx, plag
SR 479-3.7	688	890	1273.7 (4178.7)	Phyllosilicate, narrow, 2.245 strong 2.317		2:1 clay, pyx, plag
SR 499-3.7	745	911	1334.9 (4379.7)	Zeolite (Clinoptilolite or Stilbite)	Too small and friable for thin section or XRD	
SR 503-1.3	758	915	1346.4 (4417.3)	Zeolite (Analcime)	Fig 8c, 8d, zeolite	2:1 clay, pyx, plag, huelandite, analcime ✓
SR 505-7.2	770	918	1354.3	Unaltered pyroxene, weak		2:1 clay,

			(4443.2)	alteration like 425, 465		olv, pyx, phillipsite
SR 513-8.6	187	926	1379.1 (4524.6)	Zeolite (Natrolite family)	8e, smectite, zeolite, high birefringe phase	2:1 clay, pyx, plag, phillipsite, analcime, natrolite ✓
SR 537-7.4	282	951	1451.9 (4763.4)	Phyllosilicate, strong 2.314, weak 2.397	Fig 8f, altered groundmass, zeolite	2:1 clay, pyx, plag ✓
SR 541-3.6	293	955	1462.9 (4799.6)	Unaltered + Zeolite(cin/stil)+phyll(2.245,2.317)	Fig 8g, olv groundmass, smectite, zeolite	2:1 clay, pyx, plag, phillipsite
SR 544-3.0	309	958	1471.9 (4829)	Phyllosilicate (2.31, 2.36)		2:1 clay, pyx, plag
SR 560-5.7	346	976	1521.5 (4991.7)	Unaltered + phyllosilicate strong 2.314, weak 2.397		2:1 clay, pyx, plag ✓

SR 573-9.3	379	989	1562.2 (5125.3)	Similar to previous (422, 425, 465), less altered		2:1 clay, pyx, plag
SR 575-4.5	384	991	1566.8 (5140.5)	Unaltered + analcime	Fig 8h, highly altered smectite, zeolite	2:1 clay, pyx, plag, analcime
SR 612-5.8	5	1030	1680.0 (5511.8)	Similar to previous (422, 425, 465), less altered	Figure 8i, less altered, iddingsite	2:1 clay, pyx, plag
SR 614-2.9	13	1031	1685.2 (5528.9)	Similar to previous (422, 425, 465), less altered		2:1 clay, pyx, plag
SR 618-7.1	33	1036	1698.7 (5573.1)	Best example of the suite (422, 425, 465, 618), broad 2.22, strong 2.32		2:1 clay, pyx, plag ✓
SR 626-0.5	56	1044	1721.1 (5646.5)	Similar to previous (618)		2:1 clay, pyx, plag
SR 631-0.8	71	1049	1736.4 (5696.8)	Unaltered + weak zeolite	Fig 8j, 8k, chlorite?	2:1 clay, pyx, plag
SR 639-1.2	92	1057	1760.9	Zeolite (Analcime)	Fig 8l, oxide	2:1 clay,

			(5777.2)		rich, iddingsite	pyx, plag

* See the companion paper by Rasmussen et al. (in revision) for detailed presentation of XRD results.

Figures

Figure 1

PTA 2

Mauna Kea

HSDP 1

HSDP 2

SOH 2

SOH 1

SOH 4

Mauna Loa

Island of Hawaii

26.8 mi

Data LDEO-Columbia, NSF, NOAA
Data SIO, NOAA, U.S. Navy, NGA, GEBCO
Image Landsat / Copernicus
Data MBARI

Google Earth

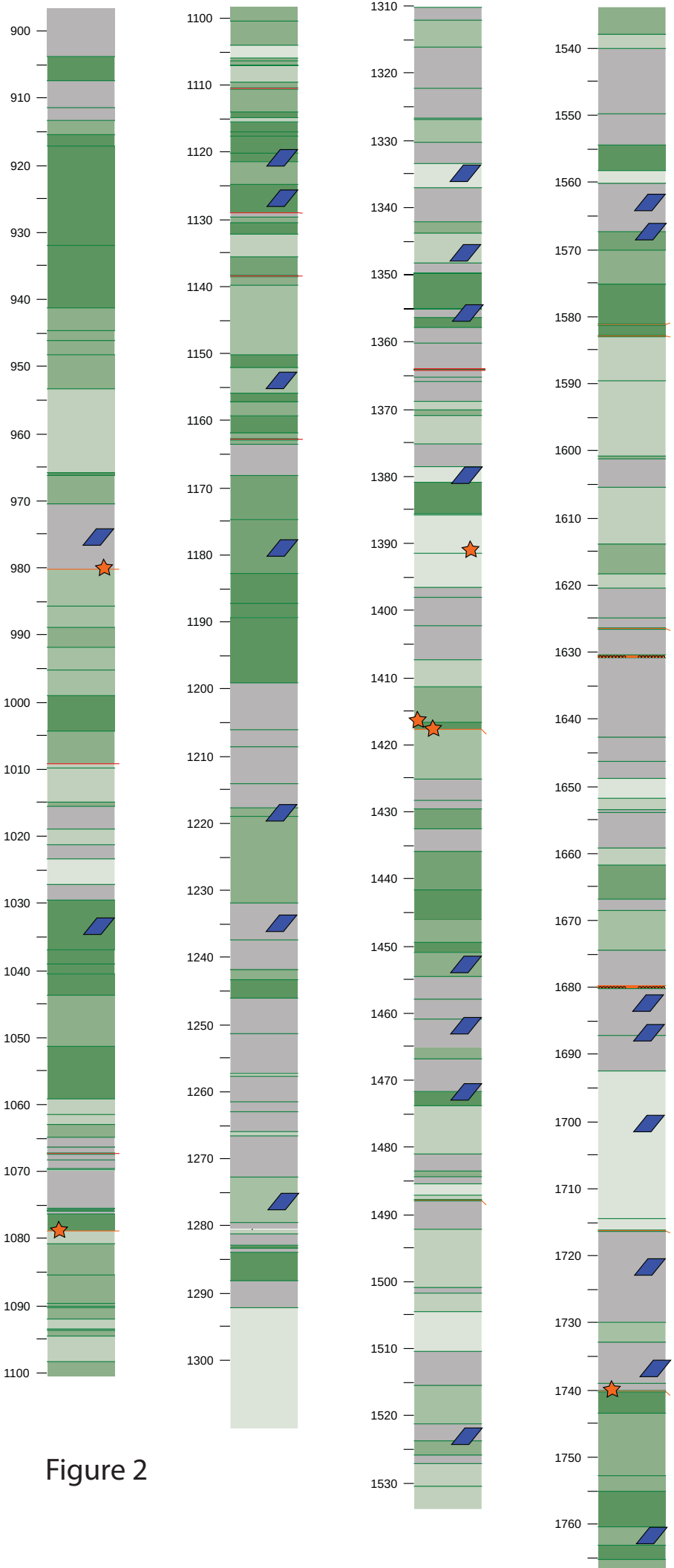
900
910
920
930
940
950
960
970
980
990
1000
1010
1020
1030
1040
1050
1060
1070
1080
1090
1100
1100
1110
1120
1130
1140
1150
1160
1170
1180
1190
1200
1210
1220
1230
1240
1250
1260
1270
1280
1290
1300
1310
1320
1330
1340
1350
1360
1370
1380
1390
1400
1410
1420
1430
1440
1450
1460
1470
1480
1490
1500
1510
1520
1530
1540
1550
1560
1570
1580
1590
1600
1610
1620
1630
1640
1650
1660
1670
1680
1690
1700
1710
1720
1730
1740
1750
1760

Figure 2

TOP

End R423

3683.5

R424

2.0

R424

3.0

R424

5.0

R425

R425

3.0

R425

5.0

R425

End R424

3688.0

R425

6.0

BOX

838

BOTTOM

Figure 3

Figure 4

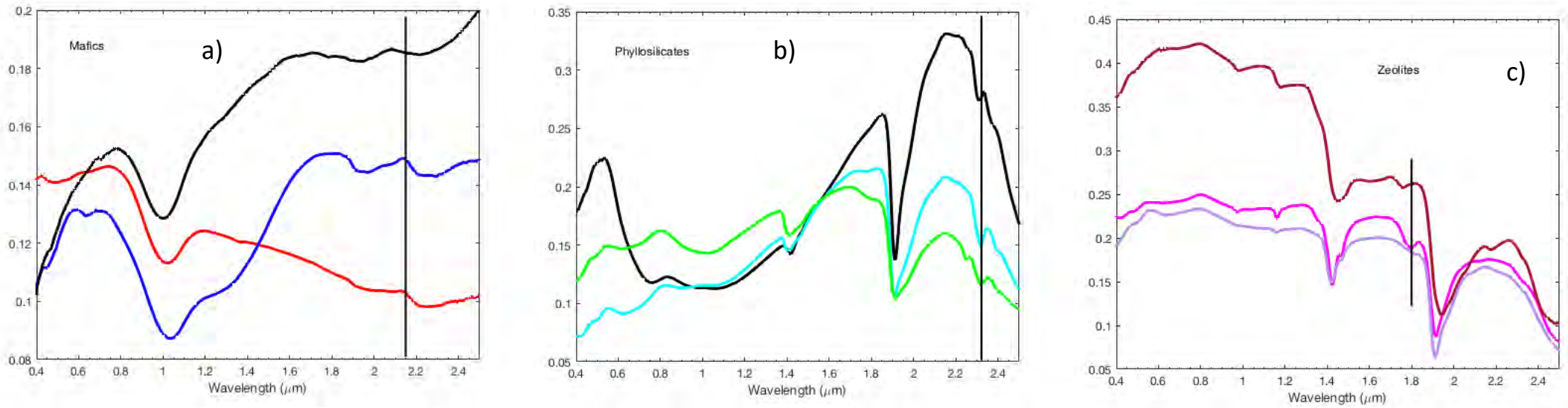
Mafics
a)
Phyllosilicates
b)
Zeolites
c)
Wavelength (μm)
Wavelength (μm)
Wavelength (μm)

Figure 5

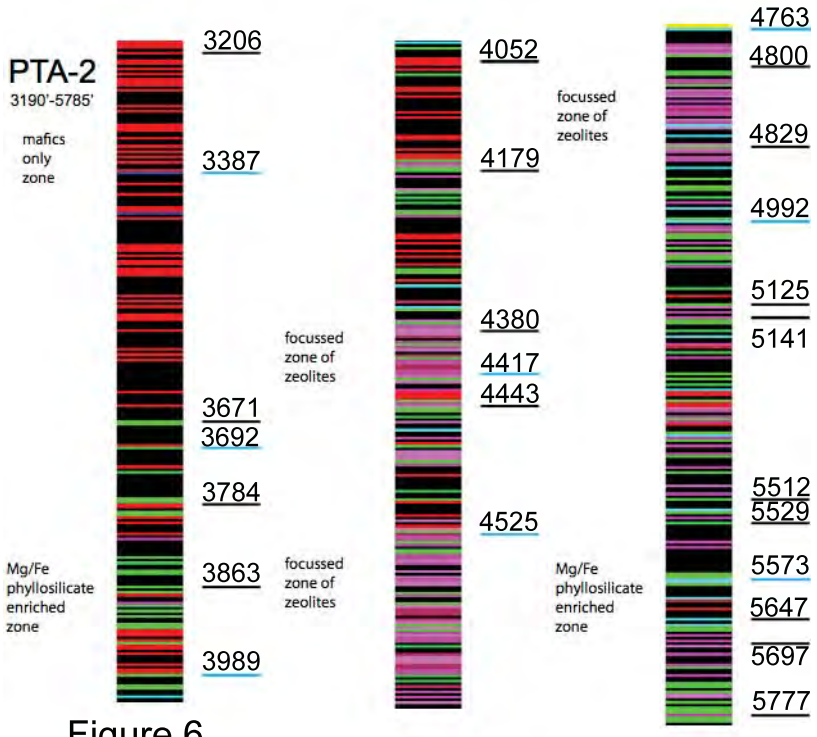
PTA-2
3190'-5785'
mafics only zone
Mg/Fe phyllosilicate enriched zone
focussed zone of zeolites
focussed zone of zeolites
focussed zone of zeolites
Mg/Fe phyllosilicate enriched zone
3206
3387
3671
3692
3784
3863
3989
4052
4179
4380
4417
4443
4525
4763
4800
4829
4992
5125
5141
5512
5529
5573
5647
5697
5777

Figure 6

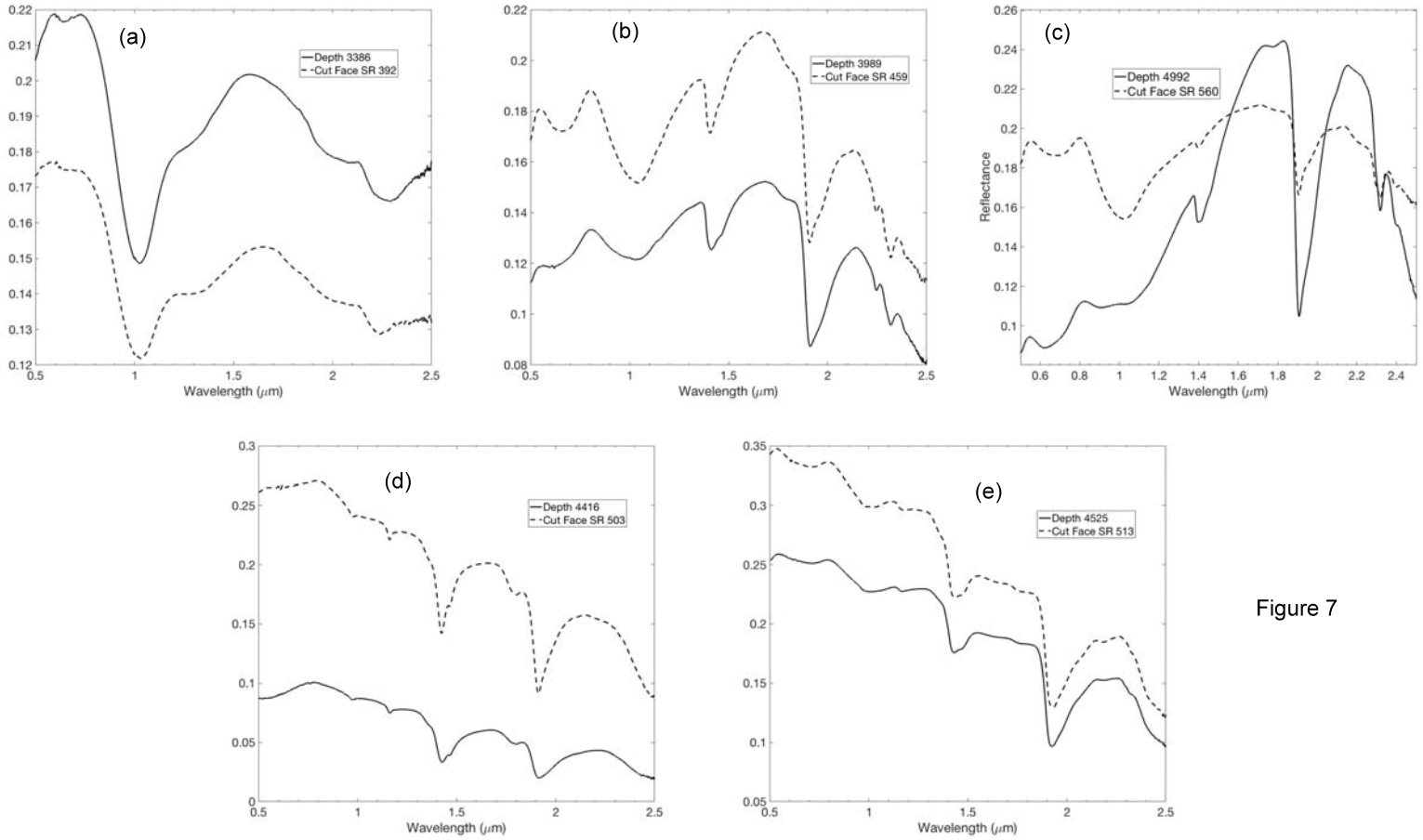
(a)
Depth 3386
Cut Face SR 392
Wavelength (μm)
(b)
Depth 3989
Cut Face SR 459
Wavelength (μm)
(c)
Depth 4992
Cut Face SR 560
Reflectance
Wavelength (μm)
(d)
Depth 4416
Cut Face SR 503
Wavelength (μm)
(e)
Depth 4525
Cut Face SR 513
Wavelength (μm)

Figure 7

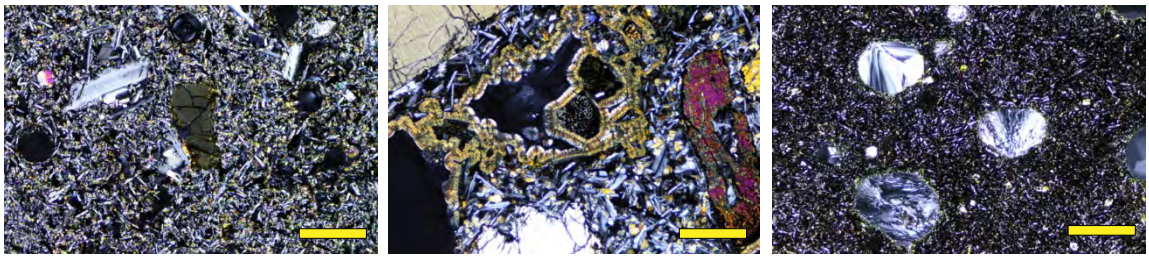

a) 977 m (2.8 mm) b) 1125.2 m (2.8 mm) c) 1346.4 m (2.8 mm)

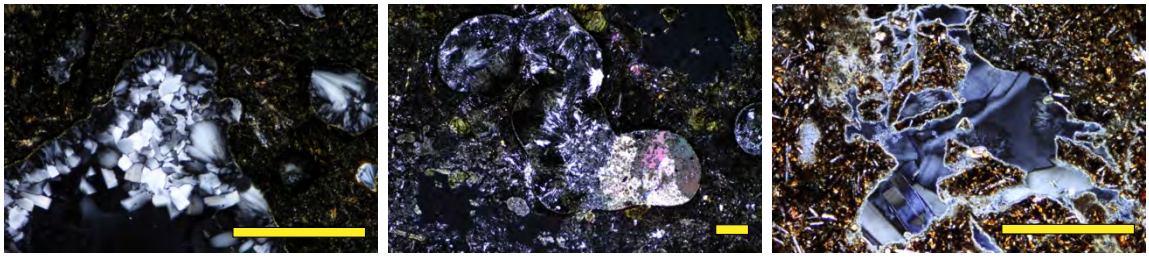

d) 1346.4 m (1.4 mm) e) 1379.1 m (5.6 mm) f) 1451.9 m (1.4 mm)

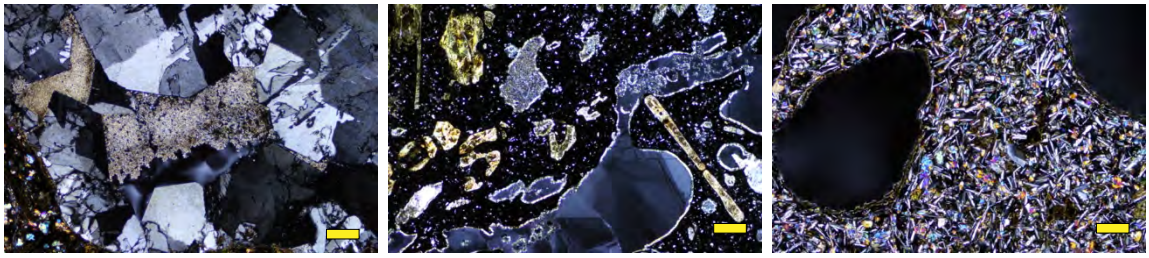

g) 1462.9 m (5.6 mm) h) 1566.8 m (5.6 mm) i) 1680.0 m (5.6 mm)

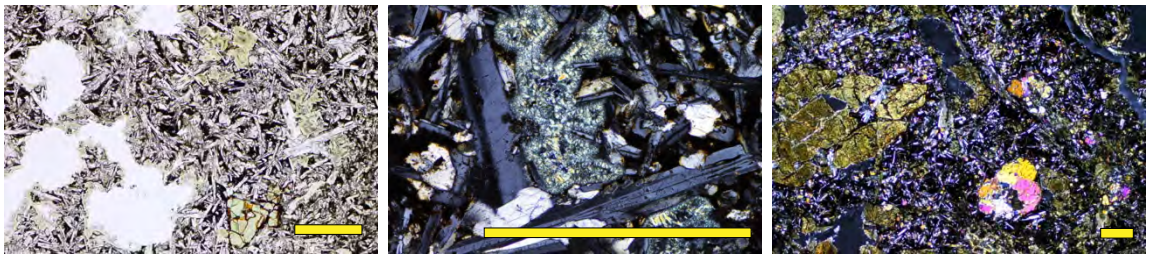

j) 1736.4 m (2.8 mm) k) 1736.4 m (0.7 mm) l) 1760.9 m (5.6 mm)

Figure 8